

Electron counting and beam-induced motion correction enable near-atomic-resolution single-particle cryo-EM

Xueming Li¹, Paul Mooney², Shawn Zheng^{1,3}, Christopher R Booth², Michael B Braunfeld^{1,3}, Sander Gubbens², David A Agard^{1,3} & Yifan Cheng¹

In recent work with large high-symmetry viruses, single-particle electron cryomicroscopy (cryo-EM) has achieved the determination of near-atomic-resolution structures by allowing direct fitting of atomic models into experimental density maps. However, achieving this goal with smaller particles of lower symmetry remains challenging. Using a newly developed single electron-counting detector, we confirmed that electron beam-induced motion substantially degrades resolution, and we showed that the combination of rapid readout and nearly noiseless electron counting allow image blurring to be corrected to subpixel accuracy, restoring intrinsic image information to high resolution (Thon rings visible to ~3 Å). Using this approach, we determined a 3.3-Å-resolution structure of an ~700-kDa protein with D7 symmetry, the *Thermoplasma acidophilum* 20S proteasome, showing clear side-chain density. Our method greatly enhances image quality and data acquisition efficiency—key bottlenecks in applying near-atomic-resolution cryo-EM to a broad range of protein samples.

Recent advancements in single-particle cryo-EM have demonstrated its capability for determining near-atomic-resolution three-dimensional (3D) structures of large protein assemblies with high symmetry, such as non-enveloped viruses with^{1–5} or, in one case, without⁶ icosahedral symmetry. This resolution is sufficient to allow the path of the polypeptide chain to be directly traced in the experimental density maps, obviating the need for prior structural information. Although, in principle, such resolutions should be obtainable for smaller macromolecular complexes or for those without high symmetry⁷, in practice, obtainable resolutions have been in the 5- to 10-Å regime, which is sufficient for docking crystal structures but not for *de novo* structure determination.

Owing to the sensitivity of the sample to radiation damage, single-particle cryo-EM requires averaging a large number of low-dose images of the same sample. For these images to be combined into a 3D reconstruction, it is necessary to determine microscope aberration parameters for each micrograph as well

as the precise 3D orientation and translation for each individual particle image. Although the quality of microscopes has steadily improved, two key limiting factors have been (i) the quality of the image-recording medium and (ii) the image blurring caused by either instability of the sample stage or motion induced by the illuminating electron beam. Given the low signal-to-noise ratio (SNR), image quality can substantially limit how accurately these parameters can be determined, hence the concern about the quality of the image detector. Of paramount importance are the efficiency of recording high-resolution information and the reduction of noise introduced by the detection process. The dominant electron image-recording media are photographic film and scintillator-based charge-coupled device (CCD) cameras. However, neither satisfies the need for both high resolution (film being better) and high-throughput image acquisition (possible only with electronic detectors).

The new generation of complementary metal-oxide semiconductor (CMOS) cameras can overcome both limiting factors. These new cameras directly detect incoming electrons in the silicon without the need for a scintillator, affording the advantages of a traditional CCD camera but with greatly improved detective quantum efficiency (DQE) at high frequency comparable to that of photographic film^{8–10}. Recent reports have characterized the performance of the DE-12 camera (Direct Electron)^{11,12} and shown that the resolution of 3D reconstructions calculated from data recorded by this camera reach a level that is close to the Nyquist limit¹¹.

Image blurring resulting from the beam striking the sample is a major limiting factor to resolution when imaging frozen hydrated biological samples¹³. In practice, beam-induced motion seems impossible to prevent^{14,15}, and it deteriorates most images from 'perfect' to marginal for high-resolution cryo-EM¹⁶. The effect can be approximated as Gaussian blurring and quantified by analogy with the crystallographic temperature factor^{17–19}, which predicts a greater-than-fivefold decrease in signal at a resolution of 3 Å (ref. 13). Thus, beam-induced motion is a major limiting factor for routine high-resolution single-particle cryo-EM.

¹The Keck Advanced Microscopy Laboratory, Department of Biochemistry and Biophysics, University of California, San Francisco (UCSF), San Francisco, California, USA. ²Gatan Inc., Pleasanton, California, USA. ³The Howard Hughes Medical Institute (HHMI), UCSF, San Francisco, California, USA. Correspondence should be addressed to D.A.A. (agard@msg.ucsf.edu) or Y.C. (ycheng@ucsf.edu).

The high frame rate (10–40 frames per second) of new CMOS-based direct cameras provides a means to correct for such image blurring by recording a ‘movie’ throughout the exposure. That is, a single exposure is fractionated into a number of subframes with sufficiently short duration such that the motion is frozen to an acceptable level¹³. The drawback is that although the signal decreases with fractionation, the camera readout noise on each subframe remains constant¹⁵. Even so, in the case of large objects such as viruses^{20,21} or ribosomes²², it has been possible to use the subframes during the refinement as if they were independent images, resulting in an increase in resolution. However, for smaller objects, the much lower SNR of each particle within a single subframe compromises the ability to accurately determine particle orientation. For this reason, we used a detector that minimizes both detection and readout noise, and we chose to correct beam-induced motion at the level of either the whole frame or large fractions of a frame.

Although direct detection substantially improves detection efficiency, a statistically varying amount of energy is deposited for each electron event (Landau noise), adding noise to the otherwise high-quality detection process. To surmount this problem, the K2 Summit direct electron-detection camera (Gatan) was designed to allow practical detection of individual electron events, thereby eliminating the Landau noise problem^{23,24}. This requires a rapid frame rate and a fast electron-detection algorithm to minimize the counting of two electrons striking the same pixel in quick succession as a single event (an error known as coincidence loss). The K2 camera has a fixed internal frame rate of 400 frames per second and the ability to find the centroid of the electron peak to subpixel accuracy (super-resolution mode). Once detected, individual electron events are then digitally accumulated over time. Because the K2 counts the primary electrons rather than simply integrating charge, as is done in other direct detection and traditional CCD cameras, both the Landau noise and the readout noise of the detector can be effectively rejected, thereby dramatically improving the DQE.

Here we demonstrate that the K2 operated in electron-counting mode is superior to both photographic film and traditional CCD cameras for imaging frozen hydrated samples. Most notably, the near-noiseless readout allows for accurate registration of dose-fractionated subframes collected throughout the exposure to correct for beam-induced motion. To aid in the correction, we developed an algorithm that maximizes the self-consistency of

the derived image shifts. With this method, we determined an $\sim 3.3\text{-\AA}$ -resolution 3D reconstruction of an archaeal 20S proteasome ($\sim 700\text{ kDa}$ and having dihedral D7 point group symmetry), which is substantially smaller in size and lower in symmetry than those of icosahedral viruses.

RESULTS

DQE and linearity of the K2 Summit

We determined the DQEs of the K2 Summit in both the conventional charge-accumulation (linear) mode and the super-resolution counting mode (Fig. 1a). As expected, the DQE in K2 counting mode was significantly higher at all spatial frequencies than those of either the K2 in linear mode or a well-characterized scintillator-based camera²⁵.

The finite internal readout rate limits the maximum electron dose rate that can be tolerated for successful counting. To investigate this, we measured the relationship between the input electron dose rate, in electrons per pixel per second ($\text{electrons pixel}^{-1}\text{ s}^{-1}$), and the camera readout rate, in counts per pixel per second ($\text{counts pixel}^{-1}\text{ s}^{-1}$) (Fig. 1b). At a dose rate up to five electrons $\text{pixel}^{-1}\text{ s}^{-1}$, the response was very close to linear, with a slope approximating the very low-dose quantum efficiency (measured as 87%). At higher dose rates, undercounting increased, with the additional coincidence loss of $\sim 11\%$ at 10 electrons $\text{pixel}^{-1}\text{ s}^{-1}$ rising to $\sim 29\%$ at 32 electrons $\text{pixel}^{-1}\text{ s}^{-1}$. The measured data are well fit with a polynomial curve (Fig. 1b), which was used to determine the exact dose rate used for each image. We limited the dose rate used in our data acquisition to between 8 and 10 electrons $\text{pixel}^{-1}\text{ s}^{-1}$.

Motion correction with dose-fractionated imaging

The optimal dose rate determined above requires a prolonged exposure time to record an image in order to achieve a targeted total dose, such as 20–30 electrons per \AA^2 and image quality could be compromised by sample-stage drift. To overcome this problem, we broke the total exposure into a stack of subframes and then mitigated image blurring by aligning all subframes within one exposure, an approach previously proposed but not fully tested¹³. As indicated above, accurate alignment is greatly facilitated by the nearly noiseless recording made possible by single-electron detection and digital accumulation on the K2 camera. Although our initial thought was to simply correct mechanical drift during the long exposures, it became apparent

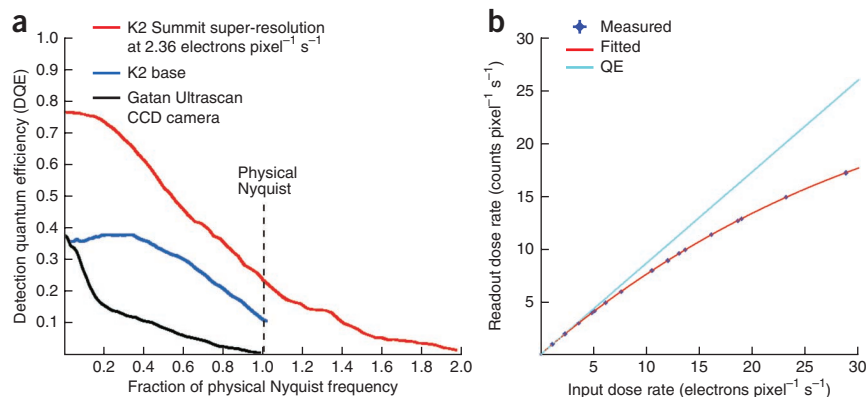
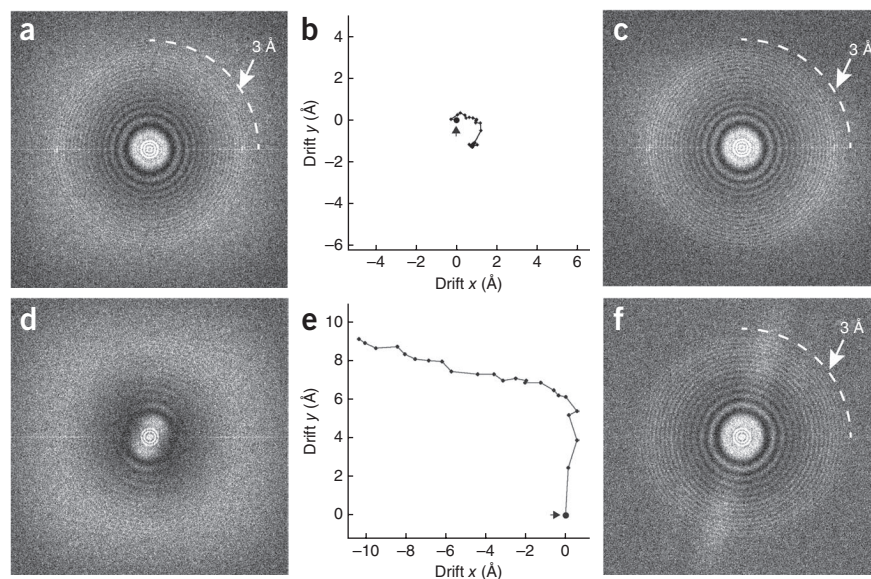


Figure 1 | Detective quantum efficiency (DQE) and detector conversion efficiency (DCE) of the K2 Summit electron-counting camera. (a) DQEs of the K2 Summit camera were measured in both counting (red, taken at 2.36 electrons $\text{pixel}^{-1}\text{ s}^{-1}$) and linear charge-accumulation modes (blue) and are compared with the DQE of a typical scintillator-based CCD camera, the Gatan US4000 Ultrascan (black). (b) Dose-dependent DCEs of the K2 Summit camera in counting mode. Electron counts were measured as a function of incident electron dose rates and were fit to a polynomial curve. The straight line represents the ideal linear response with a slope of 0.87, corresponding to the quantum efficiency (QE) of the camera.

Figure 2 | Motion correction restores the lost high-resolution information. **(a)** Fourier transforms of an image of frozen hydrated archaeal 20S proteasomes. Representative 'near-perfect' image in which Thon rings extend to nearly 3 Å. The cross-correlation (CC) between image Thon rings at 5–10 Å and simulated ideal Thon rings over the same resolution range is 0.192. **(b)** The 24 individual subframes used to create **a** were cross-correlated, and relative positional shifts were determined as described in the text and Online Methods. On the basis of these calculations, the path of motion between the first (large black dot with arrow) and last subframes can be determined. **(c)** Fourier transform of **a** after motion correction, where the Thon ring CC is 0.233. **(d)** Fourier transform of a representative imperfect image showing a predominantly unidirectional resolution cutoff at ~20 Å. The Thon ring CC is only 0.092. **(e)** Trace of detected motion between subframes used to create **d**. **(f)** Fourier transform of **d** after motion correction, showing that resolution has been isotropically restored; the Thon ring CC improved to 0.238. The narrow white band was caused by residual fixed-pattern noise in each subframe, which was subsequently eliminated.



that beam-induced blurring was a major problem and that it could also be effectively compensated.

We developed an algorithm to align all subframes that exploits redundant information between nonadjacent subframes to obtain robust subpixel accuracy (Online Methods). To explore how well induced motion could be corrected in images of frozen hydrated protein samples having low levels of contrast, we used the recombinant archaeal 20S proteasome from *T. acidophilum* as our test specimen. Its crystal structure has been determined to 3.4-Å resolution (Protein Data Bank (PDB): 1PMA)²⁶, and our best previous 3D reconstruction of the same protein was at ~5.6 Å, using photographic film²⁷.

We recorded images from our Tecnai Polara (FEI) using the K2 in super-resolution counting mode at a magnification of 31,000 \times , which corresponds to a physical pixel size of 1.22 Å. The beam intensity was set to about eight counts per physical pixel per second, corresponding to a dose rate of ~10.5 electrons per physical pixel per second on camera. Images were recorded as stack of 24 subframes, each of which was accumulated for 0.2 s, resulting in an average of ~1.7 counts per physical pixel in each subframe and a total specimen dose of ~35 electrons per Å².

We collected 553 super-resolution image stacks and used 126,729 particles for the final 3D reconstruction. For each image stack, we generated an uncorrected image, which is the direct summation of all subframes without alignment, and a corrected image after alignment. Among the entire data set, only a few images showed no obvious signs of motion-induced image blurring or resolution loss. Even for such nearly perfect images (Fig. 2a), small motion was apparent (Fig. 2b and Supplementary Fig. 1), and motion correction did slightly improve high-resolution information (Fig. 2c). At a defocus of ~1 μm, this image had excellent contrast (Supplementary Fig. 1a).

Unlike the rare near-perfect images, the majority of uncorrected images showed clear motion-induced deterioration of high-resolution signal (Fig. 2d). The calculated frame-displacement trace shows that the motion was large and not unidirectional (Fig. 2e);

this, the speed of the motion and the fact that the Polara has a stable stage all suggest that the observed motion was mostly beam induced rather than due to mechanical instability. Motion correction yielded a very symmetrical Fourier transform in which Thon rings were seen to 3-Å resolution in all directions (Fig. 2f), demonstrating that the subframe alignments were sufficiently accurate to restore high-resolution information to a degree previously possible only in the rare perfect images. Only 4 out of a total of 553 images had a total accumulated motion of ~4 Å or less, whereas the majority had a total motion of more than 10 Å during the 5-s exposure (Supplementary Fig. 2). Additionally, when we used CTFIND²⁸, it was evident that cross-correlations between high-resolution Thon rings of images and simulations were substantially improved for all motion-corrected images (Supplementary Fig. 3). Thus, motion correction allowed a large portion of images that would otherwise be discarded to be rescued, essentially making every collected image usable.

More important is the impact of motion correction on the actual 3D reconstruction (Fig. 3). We determined 3D reconstructions using both uncorrected and corrected images. With the uncorrected data, we could obtain a map with a nominal resolution around 4.2 Å (Fig. 3a), which was a dramatic improvement over the best resolution ever achieved for this sample on film (5.6 Å), demonstrating the high quality of K2 images. Correcting the beam-induced motion for all subframes with a single shift allowed us to further improve the resolution to 3.5 Å and resulted in a 3D density map with better high-resolution features (Supplementary Fig. 4). A comparison of the Fourier power spectrum calculated from these two 3D reconstructions also showed a substantial improvement in Fourier amplitude corresponding to a reduction in temperature factor of the 3D reconstruction¹⁸ (Fig. 3b).

Beam-induced motion in the frozen hydrated specimen

Although assuming that the entire subframe responds equivalently allows the majority of the motion to be corrected, previous work²⁰ has demonstrated that the motion is nonuniform. To explore

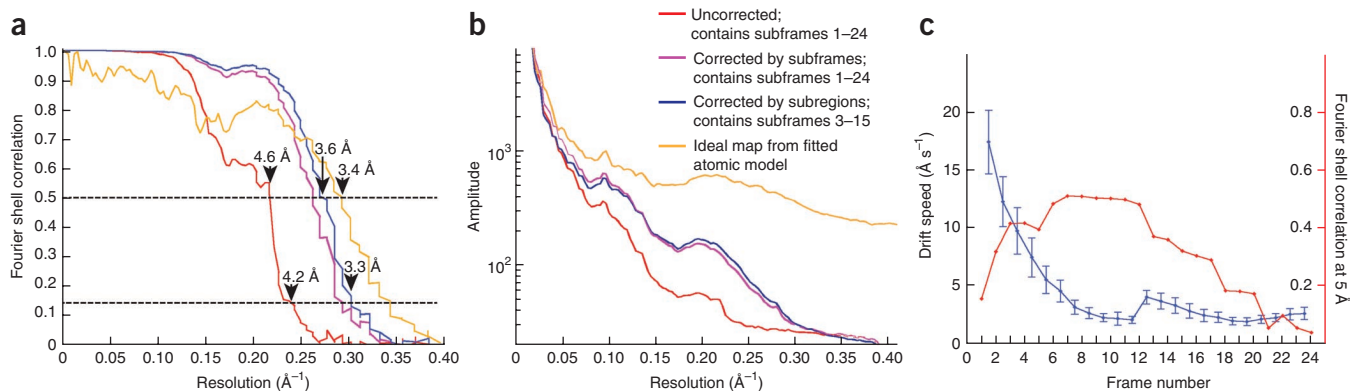


Figure 3 | Analysis of motion-induced image blurring on resolution of the 3D reconstruction. **(a)** Comparison of Fourier shell correlation (FSC) curves from 3D reconstructions using images without motion correction (red), images corrected using the entire subframe and containing all subframes (purple) and images corrected by subregion and containing subframes 3–15 (blue). Horizontal dashed lines are shown for both the FSC = 0.5 and 0.143 criteria. The FSC curve between the final map and that calculated from the fitted atomic model is shown in orange. **(b)** Comparison of rotational averages of Fourier power spectra of the different 3D reconstructions. **(c)** Average speed of motion from the entire data set of 553 images versus subframe number (blue). Error bars indicate s.d. of each average. Note the roughly exponential decay of initial motion as the sample equilibrates in the electron beam. The quality of 3D reconstructions calculated using particle data taken from the indicated individual subframes was quantified by the FSC value at 5- \AA resolution (red) derived from **Supplementary Figure 5a**. The same particle parameters were used for all 24 3D reconstructions.

the ability to accurately correct more local motions, we further divided each subframe area into a number of regions and determined the motion of each region (**Fig. 4**). For the sample and data set used here, the smallest region for which the alignment could stably be determined was about 2,000 pixels \times 2,000 pixels. As expected, in many images, motions in different areas were substantially different (**Fig. 4b,e**). However, such differences typically became small after a few subframes (**Fig. 4c,f**). Indeed, analysis of the 553 images showed that motion was fast in the beginning of the exposure and that it slowed down quickly (**Fig. 3c**). Thus, discarding the first five subframes would result in an appreciably smaller average image motion of $<1 \text{ \AA}$ in the 0.2-s accumulation used here (**Supplementary Fig. 2**). A similar observation was

described previously, but the magnitude of motion in the first few subframes was considerably larger²¹.

Whereas beam-induced motion is largest in the first few frames, beam-induced sample damage is at a minimum there. To ascertain the high-resolution information content across the entire exposure, we calculated 24 3D reconstructions using particle images from each single subframe out of the image stack and the same reconstruction parameters, which were based on refinement against the complete corrected images (**Supplementary Fig. 5**). The Fourier shell correlation (FSC) curves (**Supplementary Fig. 5a**) show that the resolution initially increased, corresponding to the decreased speed of image motion, and then decreased after the 15th subframe, owing to accumulated radiation damage.

Figure 4 | Subregion motion correction.

(a) An image of vitreous ice-embedded 20S proteasomes taken completely within a single hole of the sample grid. Black and blue squares represent two different subregions of 2,048 pixels \times 2,048 pixels. **(b)** Comparison of displacement traces determined from the two subregions in **a** (black and blue) with that determined using the entire subframe (red). Note that the trends of motions in the subregions are similar, although their speeds in the first few subframes are different. **(c)** Subframe displacement traces from the image in **a** after removal of the first five frames. The difference between two regions is substantially less than that in **b**. **(d)** Image of the same sample as in **a** but spanning both the hole and the surrounding supporting carbon film. **(e)** Comparison of displacement traces from subregions of carbon film and vitreous ice indicate that they behave differently under the electron beam. **(f)** Subframe displacement traces from the image in **d** after removal of the first five frames. After removal of the first five subframes, the remaining shifts are similarly reduced.

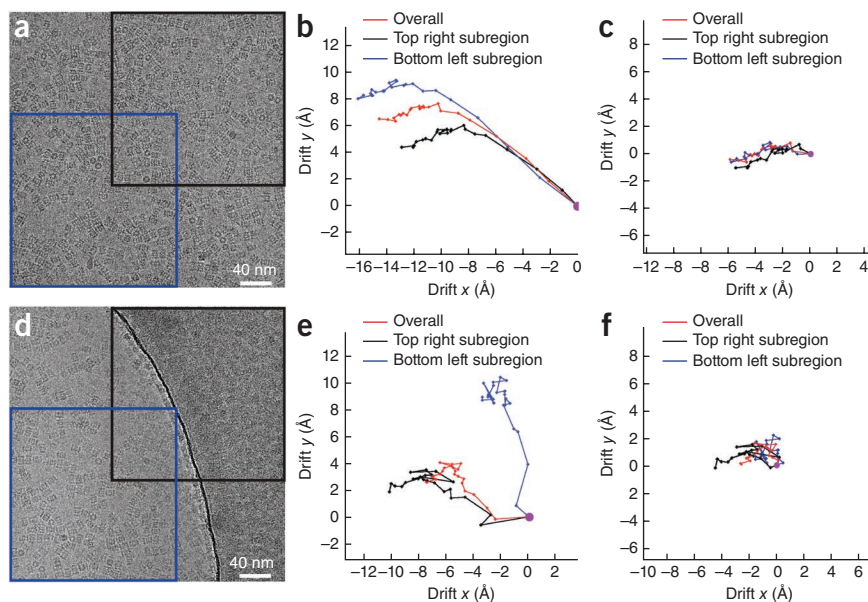
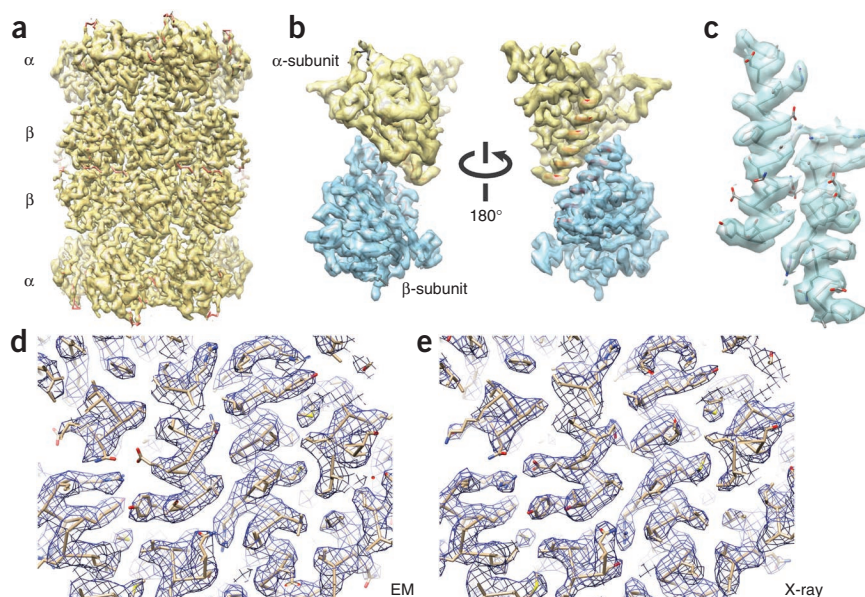


Figure 5 | Final 3D reconstruction of the *T. acidophilum* archaeal 20S proteasome. (a) 3D density map of 20S proteasome filtered to a resolution of 3.3 Å. (b) Two different views of asymmetrical α - and β -subunits segmented from the 3D density map in a. The main chain can be traced throughout the entire map. (c) Two α -helices segmented from the α - and β -subunits showing clear density for the majority of side chains. (d) Portion of the cryo-EM density map showing clear side-chain densities. The docked atomic structure was refined to fit the density map by a molecular dynamic flexible fitting procedure. (e) The same portion of a $2F_o - F_c$ map of 3.4-Å crystal structure calculated using the atomic structure (PDB: 1PMA).



The FSC values at 5 Å of each single-frame 3D reconstruction correlate well with the average motion speed (Fig. 3c).

3D reconstruction of an archaeal 20S proteasome

To obtain the best reconstruction of the *T. acidophilum* 20S proteasome, we corrected beam-induced motions using 3×3 sub-regions of 2,048 pixels \times 2,048 pixels each and then refined the 3D reconstruction using a frequency-limited refinement procedure²⁹ (Supplementary Fig. 6a and Online Methods). We further excluded the first two subframes (deteriorated by fast motion) and last ten subframes (deteriorated by radiation damage) from our calculation of the final 3D reconstruction. Our final 3D reconstruction had a nominal resolution of 3.3 Å (Fig. 3a) and was based on a total dose of ~ 17.5 electrons per Å², although the full dose of 35 electrons per Å² was used for particle refinement. This nominal resolution was confirmed by the gold-standard FSC²⁹ (Supplementary Fig. 6b). This 3D reconstruction, its FSC curve and the rotational average of its Fourier power spectrum were noticeably better than those calculated from all subframes and using the entire subframe for motion correction (Fig. 3 and Supplementary Fig. 4c). Although the difference in amplitude between the red and blue curves (that is, reconstructions calculated with uncorrected versus optimally corrected subframes; Fig. 3b) is not well represented by a single exponential falloff (*B* factor), the equivalent *B*-factor improvement ranges from ~ 100 Å² at a resolution of 10 Å to ~ 50 Å² at 5 Å. In the 3D density map (Fig. 5a–c), the C α main chain can be traced unambiguously, and most side chain densities are well resolved, validating the nominal resolution estimated from the FSC curve (Fig. 3a). The atomic structure including most of side chains of the 20S proteasome fits well into the final 3D density map, except for a small reverse turn loop of three residues in the β -subunit (Met22, Glu23 and Asn24). These residues have much higher temperature factors in the 3.4-Å crystal structure and can be remodeled to fit nicely into the density map (Supplementary Fig. 7). The overall quality of the cryo-EM 3D density map is similar to that of a 3.4-Å $2F_o - F_c$ map from the crystal structure (Fig. 5d,e). The nominal resolution, as well as the overall quality of the density map, is similar to that of several recently obtained reconstructions of much larger icosahedral viruses having much higher internal symmetry².

DISCUSSION

Here we show that the combination of a single-electron counting detector and a motion-correction algorithm make high-resolution structures obtainable by cryo-EM for smaller and lower-symmetry samples than had been previously possible. Our 3.3-Å structure of the *T. acidophilum* 20S proteasome (Fig. 5c) is comparable in resolution and map quality to the crystal structure (3.4 Å, Fig. 5e), strongly indicating the power of single-particle cryo-EM for detailed structural biology.

We showed that an electron-counting camera is superior to both photographic film and linear types of digital cameras. Its benefits derive from improved DQE at high resolution (demonstrated by the ~ 3 -Å Thon rings; Fig. 2) and excellent DQE at low resolution (allowing small proteins to be imaged at the relatively low defocusses favorable for high resolution). In this study, images of the 20S proteasome showed excellent contrast even when recorded at a defocus of ~ 1 μ m at 300 kV (Supplementary Fig. 1). Obtaining such contrast in images recorded under similar conditions was impossible when using either photographic film²⁷ or a scintillator-based CCD camera³⁰.

The other critical advantage of an electron-counting camera is the combination of essentially noiseless imaging and a high-output frame rate. Together these enable optimal collection and alignment of dose-fractionated data without the information loss inherent to any charge-accumulating camera. This not only provides a means for motion correction but also enables a better understanding and treatment of beam-induced motion, which is one of the most challenging physical problems in cryo-EM^{13–15}. Without correction, the vast majority of images were deteriorated by beam-induced motions, and only a small fraction ($\sim 1\%$) could be characterized as close to perfect. Motion correction improved the quality of almost all images (Supplementary Fig. 3), and Thon rings from a large number of corrected images could be seen at close to 3 Å (Fig. 2), which is comparable to or better than the image quality of icosahedral virus samples recorded on photographic film². Ideally, beam-induced motion should be corrected at the individual particle level during refinement of the 3D reconstruction, as demonstrated recently²¹. However, even using

electron counting, the SNR of a single 20S proteasome particle in a single subframe is much too low to permit accurate alignment. Instead, we used subregion motion correction and rejection of the first few subframes to improve local motion correction.

Potentially, the correction of beam-induced motion can be further improved. Our results indicated that the motion speed is very high in the first few subframes and that removing these subframes resulted a better 3D reconstruction. However, the specimen is least damaged by electron-beam radiation during the first fractions of an exposure³¹. A shorter subframe accumulation time would reduce motion blurring captured within each subframe and might thus rescue the discarded first few subframes. We tested this with a small image set in which 5-s-exposure images were fractionated into 50 subframes that each had an average of ~0.8 counts per pixel. The beam-induced motions were correctable (**Supplementary Figs. 8 and 9**), but at the expense of considerably more computation and data storage space. It will be worth exploring combining our approach (using finer dose-fractionated subframes) with that described by ref. 21 (averaging adjacent subframes and estimating the motion trajectory).

The final 3D reconstruction presented here was calculated from ~120,000 particles having D7 symmetry, which is many more than theoretically predicted⁷. Although high resolution can be achieved with many fewer particles (**Supplementary Fig. 10**), particle alignments were from the full data set. It may be possible to mitigate this effect by recording images with more subframes and a much higher total electron dose to boost the low-resolution amplitudes for better alignment while using only the early subframes for the reconstruction. With this and other improvements, it should be possible to get much closer to theoretical predictions.

In conclusion, by combining an electron-counting camera with dose fractionation and correction of motion-induced image blurring, we have achieved a near-atomic resolution reconstruction of an ~700 kDa protein with only D7 symmetry. The motion correction greatly enhanced high-resolution data acquisition efficiency and should facilitate the application of near-atomic-resolution single-particle cryo-EM to a broad range of protein samples.

METHODS

Methods and any associated references are available in the [online version of the paper](#).

Accession codes. The density map has been deposited in EMDDataBank ([EMD-5623](#)).

Note: Supplementary information is available in the online version of the paper.

ACKNOWLEDGMENTS

We thank K. Egami (UCSF) for purifying *T. acidophilum* 20S proteasome. We thank B. Lee for support in system optimization and DQE analysis and T. Sha for support in integrating the camera into the UCSF software environment. M. Lent was a principal architect of the camera and supported testing and troubleshooting of our prototype camera. This work is supported by the HHMI (D.A.A.) and US National Science Foundation grant DBI-0960271 to D.A.A. and Y.C., which in part funded the development of the K2 camera in association with Gatan and P. Denes at Lawrence Berkeley Labs. An initial grant from the HHMI funded the first pixel prototype chip in collaboration with P. Denes. This work is also supported by the UCSF Program for Breakthrough Biomedical Research and US National Institutes of Health grants R01GM082893, R01GM098672 and S10RR026814 to Y.C. and P50GM082250 to A. Frankel.

AUTHOR CONTRIBUTIONS

X.L., D.A.A. and Y.C. designed experiments. X.L. carried out all experiments. P.M. and C.K.B. determined DQE curves (**Fig. 1a**). S.Z. participated in implementing the K2 and dose fractionation. S.G. was the chief architect of the K2 project and, along with P.M., contributed significant scientific and technical insights throughout the project. All of the data in **Figure 1a** were collected at UCSF, and all of the other figures are based solely on experiments carried in the laboratories of Y.C. and D.A.A. M.B.B. provided technical assistance in operating the microscope. X.L., D.A.A. and Y.C. wrote the manuscript. All authors participated in discussion and revision of the manuscript.

COMPETING FINANCIAL INTERESTS

The authors declare competing financial interests: details are available in the [online version of the paper](#).

Reprints and permissions information is available online at <http://www.nature.com/reprints/index.html>.

- Wolf, M., Garcea, R.L., Grigorieff, N. & Harrison, S.C. Subunit interactions in bovine papillomavirus. *Proc. Natl. Acad. Sci. USA* **107**, 6298–6303 (2010).
- Zhang, X., Jin, L., Fang, Q., Hui, W.H. & Zhou, Z.H. 3.3 Å cryo-EM structure of a nonenveloped virus reveals a priming mechanism for cell entry. *Cell* **141**, 472–482 (2010).
- Chen, J.Z. *et al.* Molecular interactions in rotavirus assembly and uncoating seen by high-resolution cryo-EM. *Proc. Natl. Acad. Sci. USA* **106**, 10644–10648 (2009).
- Zhang, X. *et al.* Near-atomic resolution using electron cryomicroscopy and single-particle reconstruction. *Proc. Natl. Acad. Sci. USA* **105**, 1867–1872 (2008).
- Zhang, R. *et al.* 4.4 Å cryo-EM structure of an enveloped alphavirus Venezuelan equine encephalitis virus. *EMBO J.* **30**, 3854–3863 (2011).
- Zhang, J. *et al.* Mechanism of folding chamber closure in a group II chaperonin. *Nature* **463**, 379–383 (2010).
- Henderson, R. The potential and limitations of neutrons, electrons and X-rays for atomic resolution microscopy of unstained biological molecules. *Q. Rev. Biophys.* **28**, 171–193 (1995).
- McMullan, G., Chen, S., Henderson, R. & Faruqi, A.R. Detective quantum efficiency of electron area detectors in electron microscopy. *Ultramicroscopy* **109**, 1126–1143 (2009).
- McMullan, G. *et al.* Experimental observation of the improvement in MTF from backthinning a CMOS direct electron detector. *Ultramicroscopy* **109**, 1144–1147 (2009).
- McMullan, G., Clark, A.T., Turchetta, R. & Faruqi, A.R. Enhanced imaging in low dose electron microscopy using electron counting. *Ultramicroscopy* **109**, 1411–1416 (2009).
- Bammes, B.E., Rochat, R.H., Jakana, J., Chen, D.H. & Chiu, W. Direct electron detection yields cryo-EM reconstructions at resolutions beyond 3/4 Nyquist frequency. *J. Struct. Biol.* **177**, 589–601 (2012).
- Milazzo, A.C. *et al.* Initial evaluation of a direct detection device detector for single particle cryo-electron microscopy. *J. Struct. Biol.* **176**, 404–408 (2011).
- Henderson, R. & Glaeser, R.M. Quantitative analysis of image contrast in electron micrographs of beam-sensitive crystals. *Ultramicroscopy* **16**, 139–150 (1985).
- Glaeser, R.M., McMullan, G., Faruqi, A.R. & Henderson, R. Images of paraffin monolayer crystals with perfect contrast: minimization of beam-induced specimen motion. *Ultramicroscopy* **111**, 90–100 (2011).
- Typeke, D., Gilpin, C.J., Downing, K.H. & Glaeser, R.M. Stroboscopic image capture: reducing the dose per frame by a factor of 30 does not prevent beam-induced specimen movement in paraffin. *Ultramicroscopy* **107**, 106–115 (2007).
- Miyazawa, A., Fujiyoshi, Y., Stowell, M. & Unwin, N. Nicotinic acetylcholine receptor at 4.6 Å resolution: transverse tunnels in the channel wall. *J. Mol. Biol.* **288**, 765–786 (1999).
- Jensen, G.J. Alignment error envelopes for single particle analysis. *J. Struct. Biol.* **133**, 143–155 (2001).
- Rosenthal, P.B. & Henderson, R. Optimal determination of particle orientation, absolute hand, and contrast loss in single-particle electron cryomicroscopy. *J. Mol. Biol.* **333**, 721–745 (2003).
- Saad, A. *et al.* Fourier amplitude decay of electron cryomicroscopic images of single particles and effects on structure determination. *J. Struct. Biol.* **133**, 32–42 (2001).

20. Brilot, A.F. *et al.* Beam-induced motion of vitrified specimen on holey carbon film. *J. Struct. Biol.* **177**, 630–637 (2012).
21. Campbell, M.G. *et al.* Movies of ice-embedded particles enhance resolution in electron cryo-microscopy. *Structure* **20**, 1823–1828 (2012).
22. Bai, X.-c., Fernandez, I.S., McMullan, G. & Scheres, S.H.W. Ribosome structures to near-atomic resolution from thirty thousand cryo-EM particles. *ELife* **2**, e00461 (2013).
23. Battaglia, M. *et al.* A rad-hard CMOS active pixel sensor for electron microscopy. *Nucl. Instrum. Methods Phys. Res. A* **598**, 642–649 (2009).
24. Bichsel, H. Straggling in thin silicon detectors. *Rev. Mod. Phys.* **60**, 663–699 (1988).
25. Booth, C.R., Jakana, J. & Chiu, W. Assessing the capabilities of a 4kx4k CCD camera for electron cryo-microscopy at 300 kV. *J. Struct. Biol.* **156**, 556–563 (2006).
26. Löwe, J. *et al.* Crystal structure of the 20S proteasome from the archaeon *T. acidophilum* at 3.4 Å resolution. *Science* **268**, 533–539 (1995).
27. Rabl, J. *et al.* Mechanism of gate opening in the 20S proteasome by the proteasomal ATPases. *Mol. Cell* **30**, 360–368 (2008).
28. Mindell, J.A. & Grigorieff, N. Accurate determination of local defocus and specimen tilt in electron microscopy. *J. Struct. Biol.* **142**, 334–347 (2003).
29. Scheres, S.H. & Chen, S. Prevention of overfitting in cryo-EM structure determination. *Nat. Methods* **9**, 853–854 (2012).
30. Yu, Y. *et al.* Interactions of PAN's C-termini with archaeal 20S proteasome and implications for the eukaryotic proteasome-ATPase interactions. *EMBO J.* **29**, 692–702 (2010).
31. Stark, H., Zemlin, F. & Boettcher, C. Electron radiation damage to protein crystals of bacteriorhodopsin at different temperatures. *Ultramicroscopy* **63**, 75–79 (1996).



ONLINE METHODS

Motion-correction algorithm. Assuming that a dose-fractionated image stack contains n subframes, f_1, f_2, \dots, f_n , the relative shift between two adjacent subframes, f_i and f_{i+1} , is $\mathbf{r}_i = [x, y]$. The goal of any motion-correction algorithm is to accurately determine all \mathbf{r}_i ($i = 1$ to $n - 1$). A commonly used algorithm is to determine \mathbf{r}_i by locating the peak position in the cross-correlation map between two adjacent subframes f_i and f_{i+1} or between one fixed subframe and every other subframe. In these approaches, each \mathbf{r}_i is determined by only a single measurement. Although this approach is computationally efficient, it has potential disadvantages: (i) it is difficult to estimate accuracy from a single measurement; (ii) any residual fixed-noise pattern from hot or dead pixels or otherwise imperfect dark current correction will generate a strong cross-correlation peak in the center of correlation maps, which can overshadow the real peak from image alignment; (iii) the previous problem is compounded by low signal-to-noise ratios (SNRs) that can broaden the cross-correlation peak; or (iv) a small amount of image shift between adjacent subframes that can bury the true peak in the side of a false origin peak. Thus, the accuracy of a single-measurement approach is limited by unpredictable errors caused by complicated shapes and features of the cross-correlation peak.

Instead we use redundant measurements for a more accurate and self-consistent determination of image shifts. A relative shift, \mathbf{b}_{ij} , between any two subframes, f_i and f_j , where $j > i$, is the summation of shift vectors between all intervening adjacent subframes, \mathbf{r}_i (**Supplementary Fig. 11**)

$$\mathbf{r}_i + \mathbf{r}_{i+1} + \dots + \mathbf{r}_{j-1} = \mathbf{b}_{ij} \quad (1)$$

\mathbf{b}_{ij} can be measured by locating the maximum value of the cross-correlation map, often after applying a B factor (see below), between the subframes f_i and f_j . By determining all possible image shifts between any two subframes, we generate a set of linear equations that contains $m = (n - 1)n/2$ equations such as equation (1)

$$\left\{ \begin{array}{l} \mathbf{r}_1 = \mathbf{b}_{12} \\ \mathbf{r}_1 + \mathbf{r}_2 = \mathbf{b}_{13} \\ \dots \\ \mathbf{r}_2 + \mathbf{r}_3 + \mathbf{r}_4 = \mathbf{b}_{25} \\ \mathbf{r}_2 + \mathbf{r}_3 + \mathbf{r}_4 + \mathbf{r}_5 = \mathbf{b}_{26} \\ \dots \\ \mathbf{r}_j + \dots + \mathbf{r}_{j-1} = \mathbf{b}_{ij} \\ \dots \end{array} \right. \quad (2)$$

Because the number of equations is much greater than the number of unknowns $\mathbf{r}_1, \dots, \mathbf{r}_{n-1}$, equation (2) is an overdetermined set of linear equations. It can be rewritten in a matrix form as

$$\mathbf{A}\mathbf{r} = \mathbf{b} \quad (3)$$

where \mathbf{A} is an $m \times (n - 1)$ coefficient matrix, $\mathbf{r} = [\mathbf{r}_1, \mathbf{r}_2, \dots, \mathbf{r}_{n-1}]^T$, $\mathbf{b} = [\mathbf{b}_{12}, \mathbf{b}_{13}, \dots, \mathbf{b}_{ij}, \dots]^T$ ($j > i$) and superscript T indicates transposition. A least-squares solution of \mathbf{r} can be calculated by the generalized inverse matrix method as

$$\mathbf{r}_s = (\mathbf{A}^T \mathbf{A})^{-1} \mathbf{A}^T \mathbf{b} \quad (4)$$

The residual error of each measured shift \mathbf{b}_{ij} can be calculated by

$$\Delta b = \|\mathbf{A}\mathbf{r}_s - \mathbf{b}\| \quad (5)$$

Δb can be used to qualify the accuracy of xy -shift determination. In the current study, any equation with a residual error larger than a given criterion, such as 1 pixel, is removed from equations (2) and (3) unless removing it makes \mathbf{A} become not full ranked. Afterwards, equation (4) is recalculated to get the final solution, \mathbf{r}_s . Finally, all subframes are shifted to the same origin by changing the phase in their Fourier transform. Summation of all corrected subframes produces an image in which motion-induced image blurring is corrected.

The peak position in the cross-correlation map between two subframes can be directly determined to a precision much better than 1 pixel. In the cross-correlation map, the peak position is first identified, then an area of 16 pixels \times 16 pixels around the peak is cropped out from the cross-correlation map. The Fourier transform of the cropped area is then padded to a larger area of 512 pixels \times 512 pixels, which is followed by an inverse Fourier transform, allowing the position of the cross-correlation peak to be determined by Fourier interpolation to a precision of 1/32 of a pixel. This procedure is equivalent to but computationally more efficient than the direct interpolation in the cross-correlation map by sinc function profile fitting.

Applying motion correction to images of frozen hydrated protein samples. Although the method described above is applicable to motion correction of any multisubframe image stack, applying it to dose-fractionated image stacks of frozen hydrated protein samples recorded with the K2 Summit in electron-counting mode benefits from additional considerations, including minimizing fixed-pattern noise and frame exposure time, described below.

Fixed-pattern noise. A critical factor that influences the accurate determination of small shifts is any residual fixed-pattern noise, which usually results from imperfect gain normalization and dark reference subtraction or any uncorrected dead or hot pixels on the camera. This pattern is identical in each subframe and generates a strong and sharp peak in the origin of the cross-correlation map. Under very low-dose conditions, this peak is often stronger than the real cross-correlation peak from image alignment. We used two strategies to avoid or to reduce the influence of fixed-pattern noise.

Because these problems are generally caused by individual pixels, the contribution of a fixed noise pattern to the Fourier transform is mostly beyond half the Nyquist limit. Thus, the severity of this problem can be minimized by applying a low-pass filter such as a B factor to all subframes

$$e^{-\frac{1}{2}BH^2} \quad (6)$$

where B is the factor with units of pixel² and H is the spatial frequency with units of pixel⁻¹. A B factor of 100–200 pixels² is sufficient to reduce the intensity of the sharp correlation peak corresponding to the fixed noise pattern but not to significantly influence the shape of the real cross-correlation peak from image alignment. Applying a B factor means that only low-resolution information is used for subframe alignment; however, motion

correction does restore high-resolution information in the corrected image (**Supplementary Fig. 12**).

The second strategy is to set a minimal subframe interval between any two subframes that are used for determination of \mathbf{b}_{ij} in equations (1) and (2). This is to avoid aligning a subframe with its immediate adjacent subframes, where the image shifts between such subframes are relatively small and the cross-correlation peak is very close to the peak from the fixed noise pattern.

Frame exposure time. Ideally, the subframe recording time should be kept as short as possible to minimize the uncorrectable image motion captured in each subframe. Motion within the subframe elongates the cross-correlation peak and introduces a larger error in identifying the peak position. Furthermore, fractionating the total dose into more subframes produces more equations in (2), which have the potential to reduce statistical errors. However, a shorter subframe accumulation time also reduces the average counts per pixel and thus reduces the SNR of each subframe, which in turn weakens and broadens the cross-correlation peak. Thus, for a fixed total dose, there is a limit of how many subframes can be used while maintaining a satisfactory alignment accuracy. We have tested the algorithm described above and obtained satisfactory results from fractionating ten subframes in 1 s. Under this condition, the average count per pixel is ~ 0.8 (**Supplementary Figs. 9 and 10**). With this shorter exposure, the fast beam-induced motion in the first few frames can be better corrected.

We implemented the algorithm described here in a program that runs on graphic processing units (GPUs) for fast processing. Correction of an image contains 24 subframes of $3,840 \text{ pixels} \times 3,840 \text{ pixels}$ takes $\sim 10 \text{ s}$ to complete on a single GTX580 GPU. The program is included as **Supplementary Software**.

Materials, instrumentation and data acquisition. The *T. acidophilum* 20S proteasome was expressed and purified from *Escherichia coli* according to established protocols^{27,30}. A drop of $2 \mu\text{L}$ of purified 20S proteasome at a concentration of $\sim 0.9 \mu\text{M}$ was applied to glow-discharged Quantifoil holey carbon grids (Quantifoil Micro Tools GmbH) and plunge-frozen by using a Vitrobot Mark III (FEI). Images of frozen hydrated *T. acidophilum* 20S proteasome were collected on a FEI TF30 Polara electron microscope (FEI) equipped with a field emission electron source and a Gatan K2 Summit camera. The microscope was operated at an accelerating voltage of 300 kV.

The K2 camera has $3,840 \text{ physical pixels} \times 3,840 \text{ physical pixels}$. All counting images were recorded using super-resolution mode, resulting in $7,680 \text{ super-resolution pixels} \times 7,680 \text{ super-resolution pixels}$. Fresh hardware and software flat fielding gain and hardware dark references were carefully prepared using the Gatan Microscopy Suite (GMS) for each dose rate used immediately before data acquisition. The pixel sizes at different magnifications were calibrated by using a hexagonal ice lattice at $-185 \text{ }^\circ\text{C}$. All images of frozen hydrated protein samples used here were recorded at a nominal magnification of $31,000\times$, corresponding to a physical pixel size of 1.22 \AA at the specimen level. We used UCSFImage4 to control all data acquisition. All images were recorded with a defocus in the range of $0.8\text{--}1.9 \mu\text{m}$.

Grids of frozen hydrated samples were imaged at dose rate of about eight counts per physical pixel per second for 5 s with a total specimen dose of $\sim 34 \text{ electrons per } \text{\AA}^2$. Each image was

fractionated into 25 subframes, with 0.2-s subframe accumulation time. The first subframe was discarded because of a slight delay in shutter opening that resulted in a partial exposure. After collecting 553 images, we collected 20 more images with a 5-s exposure, but these were fractionated into 50 subframes that each had 0.1-s subframe accumulation. These 20 images were not used for the 3D reconstruction but only for testing motion correction at a lower subframe dose (**Supplementary Figs. 9 and 10**). All images were saved as stacks of subframes in full resolution for later processing. An uncorrected data set was generated by direct summation of all subframes within one image stack.

Determination of DQE. DQEs of the K2 Summit in both the linear and super-resolution-counting modes were measured by knife-edge images recorded at an acceleration voltage of 300 kV. DQE was measured as described in ref. 32 and similarly to the method described in ref. 33. The method relies on the conversion of the fundamental definition of DQE as $\text{SSNR}_{\text{out}}/\text{SSNR}_{\text{in}}$ to the form $\text{MTF}^2/(\text{NPS}/\text{dose})$, where SSNR is the ratio of signal and noise power spectra, MTF is the modulation transfer function and NPS is the noise power spectrum, and on the use of an image of the shadow of a post-TEM optics edge as a source of known frequency content for the MTF measurement. Because an edge image spans a range of signal levels, detector linearity has been a precondition for the use of this method. In the case of a detector that exhibits a gradual change in detector conversion efficiency (DCE) due to changes in coincidence loss as dose is increased, dose levels need to be used at which dose dependence is small, and all measurements need to be taken at the same dose rate to ensure consistent calibration. The dose chosen for data acquisition and used for DQE measurement, 2.4 electrons per physical pixel per second, was at a level for which the deviation from linearity in the DCE curve (**Fig. 1b**) is very small. This means that the error in the edge-shadow DQE method will be small. Attempts to measure DQE at ten electrons $\text{pixel}^{-1} \text{ s}^{-1}$ and higher doses lead to overestimates caused by the nonlinearity of coincidence loss.

Determination of DCE. A series of super-resolution images without specimens were recorded at incremental dose rates from 1 to 30 counts $\text{pixel}^{-1} \text{ s}^{-1}$ by adjusting the beam intensity. Multiple measurements were taken for each data point. For each counting image, a corresponding image recorded with the K2 Summit operating in linear mode was also obtained at the same beam condition. During the image acquisition, the exposure time was also changed from 40 s at 1 count $\text{pixel}^{-1} \text{ s}^{-1}$ to 10 s at 30 counts $\text{pixel}^{-1} \text{ s}^{-1}$ to maintain a total dose of at least 40 electrons per pixel. The DCE curve shown in **Figure 1b** was obtained by plotting the averaged readout rate (counts $\text{pixel}^{-1} \text{ s}^{-1}$) from the counting image against the input dose rate (electrons $\text{pixel}^{-1} \text{ s}^{-1}$), and a polynomial curve was fitted against all data points. The input dose rate was calculated from the counts of the corresponding linear image, which we calibrated at a high dose rate, as one electron generates 30.0 ± 0.5 counts. The linear-mode calibration was measured using the Gatan GIF drift tube and Keithley 6485 picammeter set to its slowest sampling rate. Once determined, the fitted polynomial curve was used to calculate actual input dose rate from the readout count rate on camera for subsequent experiments.

The slope of the straight line in **Figure 1b** is 0.87, corresponding to the quantum efficiency (QE) determined as the slope of tangent

line of the fitted polynomial curve at the origin. Coincidence loss, which causes the camera readout to deviate from a linear relationship, was calculated as the differential between the observed counts and those expected with a finite QE.

Image processing. All super-resolution subframes were 2×2 binned for further processing. The final image pixel size is 1.22 Å. All binning was calculated using Fourier cropping, in which a Fourier transform from the original 7,680 pixel \times 7,680 pixel image was calculated and a central 3,840 pixel \times 3,840 pixel area was cropped out and followed by a reverse Fourier transform. This produced an image of 3,840 pixels \times 3,840 pixels that was 2×2 binned from the original image. Initial defocus values of each image were determined using CTFFIND3 (ref. 28) on uncorrected and 4×4 -binned data sets.

We corrected beam-induced motion in each image using the algorithm described above. For 24-subframe image stacks, the minimum subframe interval was set to 7 to avoid alignment between adjacent subframes, which could have very small shift and result in inaccurate subframe alignment. Thus, a total 138 comparison were carried out for a total 24 subframes. The corrected image stacks were evaluated by using CTFFIND3, setting the resolution range to 5–10 Å. The cross-correlation value before and after motion correction was used to monitor the motion-correction procedure.

Side-view particles of the 20S proteasome were picked automatically using FindEM³⁴. All picked particles were first subjected to standard procedures of multiple rounds of multireference alignment and classification implemented in SPIDER³⁵. Particles within bad 2D classes were discarded. Remaining bad particles were removed by further manual inspection. The final data set contains 129,008 particles. GeFREALIGN³⁶ was used to refine and determine the 3D reconstructions with D7 symmetry following a frequency-limited refinement procedure²⁹. A map calculated from the atomic structure of the archaeal 20S proteasome (PDB code: 1PMA) was used as the initial model. The Euler angles and in-plane shift were first determined by a global search followed by local refinement (mode 4 in GeFREALIGN). The resolution of the search and refinement was limited to 15 Å, and the 3D reconstruction at each cycle was calculated to the Nyquist limit. We carried out a total of five cycles of global search, local refinement and 3D reconstruction. This was followed by an additional 25 cycles of local refinement (mode 1 in GeFREALIGN). The resolution for the refinement was gradually increased to 5 Å. At this stage the resolution of 3D reconstruction had reached 3.4 Å. We continued refinement for another ten cycles with the resolution of refinement gradually increased to 3.5 Å. A total of 126,729 particles were used in the final 3D reconstruction after we rejected 2,279 particles on the basis of a phase residual cutoff. The resolutions of 3D reconstructions were estimated using Fourier shell correlation curves using FSC = 0.143 criteria¹⁸, but the resolutions corresponding to the FSC = 0.5 were also given. The final 3D reconstruction, which contains only subframes 3–15, has a resolution of 3.3 Å (Supplementary Fig. 6a).

In light of the recent development of using a ‘gold-standard’ FSC to estimate the resolution²⁹, we repeated the entire data processing by splitting the data into two half-data sets with

even- and odd-numbered particles and processed them separately. The first initial model was the same as described above, and the initial search and refinement was limited to 15 Å. The final FSC curve calculated between the two independently processed sets gave the gold-standard FSC curve, which is similar to the FSC curve obtained previously (Supplementary Fig. 6b), attesting to the high SNR in the reconstruction. We also calculated an FSC curve between the gold-standard map and the conventional map, which gave an FSC = 0.5 at 3.3 Å (Supplementary Fig. 6b). This additional test confirms the resolution we had obtained by the frequency-limited refinement procedure. All figures were prepared from the map calculated from the frequency-limited refinement method. As pointed out previously, overfitting can be prevented by either frequency-limited refinement or gold-standard procedures²⁹, so it is not surprising that the two procedures gave the same resolution.

After particle picking, we carried out subregion motion correction. Each subframe was divided into 3×3 subregions of 2,048 pixels \times 2,048 pixels with overlap, which generated nine subregions stacks. The motion correction was carried out on each subregion separately. All particles were assigned to the nearest subregion according to the distance to the centers of nine subregions and boxed out from the corrected image from the corresponding subregion. The final 3D reconstruction was calculated from the subregion motion-corrected image stack, which yielded an improved FSC. To calculate the final 3D reconstruction, we further removed the first two and the last ten subframes, using only subframes 3–15 of each subregion corrected image stack. The amplitude of the final 3D density map was scaled to the ideal density map from the atomic structure and low-pass filtered to the estimated resolution.

Docking of atomic structure. The atomic structure of *T. acidophilum* 20S proteasome was first docked as a rigid body into the 3D density map by using the fit-in-map function from UCSF Chimera³⁷. The atomic structure, including both the main chain and side chains, fits well into the final 3D density map, except for a small loop of four residues. The fitting was further refined by using the molecular dynamics flexible fitting (MDFF) procedure³⁸.

- Mooney, P. Optimization of image collection for cellular electron microscopy. *Methods Cell Biol.* **79**, 661–719 (2007).
- Meyer, R.R., Kirkland, A.I., Dunin-Borkowski, R.E. & Hutchison, J.L. Experimental characterisation of CCD cameras for HREM at 300 kV. *Ultramicroscopy* **85**, 9–13 (2000).
- Roseman, A.M. FindEM—a fast, efficient program for automatic selection of particles from electron micrographs. *J. Struct. Biol.* **145**, 91–99 (2004).
- Shaikh, T.R. *et al.* SPIDER image processing for single-particle reconstruction of biological macromolecules from electron micrographs. *Nat. Protoc.* **3**, 1941–1974 (2008).
- Li, X., Grigorieff, N. & Cheng, Y. GPU-enabled FREALIGN: accelerating single particle 3D reconstruction and refinement in Fourier space on graphics processors. *J. Struct. Biol.* **172**, 407–412 (2010).
- Pettersen, E.F. *et al.* UCSF Chimera—a visualization system for exploratory research and analysis. *J. Comput. Chem.* **25**, 1605–1612 (2004).
- Trabuco, L.G., Villa, E., Mitra, K., Frank, J. & Schulten, K. Flexible fitting of atomic structures into electron microscopy maps using molecular dynamics. *Structure* **16**, 673–683 (2008).